



Available online at www.sciencedirect.com



Computers and Mathematics with Applications 53 (2007) 547–568

An International Journal
**computers &
mathematics
with applications**

www.elsevier.com/locate/camwa

Numerical simulations of shear dependent viscoelastic flows with a combined finite element–finite volume method

Lionel Nadau, Adélia Sequeira*

Centro de Matemática e Aplicações and Departamento de Matemática, Instituto Superior Técnico, 1049-001 Lisboa, Portugal

Received 13 September 2005; accepted 27 February 2006

Abstract

A hybrid combined finite element–finite volume method has been developed for the numerical simulation of shear-dependent viscoelastic flow problems governed by a generalized Oldroyd-B model with a non-constant viscosity function. The method is applied to the 4:1 planar contraction benchmark problem, to investigate the influence of the viscosity effects on the flow and results are compared with those found in the literature for creeping Oldroyd-B flows, for a range of Weissenberg numbers. The method is also applied to flow in a smooth stenosed channel. It is shown that the qualitative behavior of the flow is influenced by the rheological properties of the fluid, namely its viscoelastic and inertial effects, as well as the shear-thinning viscosity.

These results appear in the framework of a preliminary study of the numerical simulation of steady and pulsatile blood flows in two-dimensional stenotic vessels, using this hybrid finite element–finite volume method.

© 2007 Elsevier Ltd. All rights reserved.

Keywords: Finite element–finite volume; Viscoelastic flows; Shear-dependent flows; Stenosed channel

1. Introduction

Complex rheological phenomena such as shear-thinning or shear-thickening viscosity, stress relaxation, nonlinear creeping, normal stress differences and yield stress are typically encountered in many fluids characterized by long chain molecules and complex microstructure. In particular, polymer melts, suspensions, liquid crystals or biological fluids exhibit such properties, leading to nonlinear viscoelastic behavior, which cannot be described by the classical linearly viscous Newtonian flow, and are called non-Newtonian fluids (see [1]). Striking manifestations of non-Newtonian phenomena have been observed experimentally, such as the Weissenberg or rod-climbing effect, extrudate swell or vortex growth in a contraction flow (see the monograph [2]). There are many ways to generalize the Newtonian law of viscosity by inclusion of nonlinear terms relating the Cauchy stress and the strain tensor. The simplest case is the generalized Newtonian model where the extra-stress incorporates a shear-rate dependent viscosity. However the generalized Newtonian fluids cannot account for the effects described above, namely the viscoelasticity, but they are often used to model simple flows and to study the flow rate in a pipe, as a function of the pressure drop. Suitable viscoelastic constitutive equations are then required. In general terms, non-Newtonian viscoelastic fluids exhibit both

* Corresponding author.

E-mail addresses: lionel_nadau@yahoo.fr (L. Nadau), adelia.sequeira@math.ist.utl.pt (A. Sequeira).

viscous and elastic properties and can be classified as fluids of differential type, rate type and integral type [1]. We refer to the monographs [3–5] for relevant issues related to non-Newtonian fluid behavior and modeling. Models of rate type such as Maxwell or Oldroyd-B fluids can predict stress relaxation and are used to describe flows in polymer processing. However they cannot capture the complex rheological behavior of many real fluids, such as blood in which the non-Newtonian viscosity effects are of major importance.

Blood is a multicomponent mixture of elastic cells (red blood cells, white blood cells, platelets and other matter) suspended in an aqueous polymer solution, the plasma (Newtonian fluid) containing inorganic and organic salts, proteins and transported substances. In large and medium size vessels, blood is usually modeled as a Newtonian liquid. However in smaller vessels blood behaves as a shear-thinning and viscoelastic fluid, at least at low shear rates, as experimentally recognized by Thurston [6]. Hemorheology is concerned with the deformation and flow properties of cellular and plasmatic components of blood, and with the complex phenomena contributing to the physiology and pathology of blood circulation. The investigation of mathematical models for hemorheology has emerged as an important and useful tool in supplementing experimental data and understanding the interplay of the rheological and biochemical factors under various flow conditions encountered in the human vasculature.

Generalizations of the Oldroyd-B model that can capture the shear-thinning and viscoelastic behavior of blood have been considered by several authors. The empirical three constant generalized Oldroyd-B model studied in [7] belongs to this class and has been obtained by fitting experimental data in one dimensional flows and generalizing such curve fits to three dimensions. A general thermodynamic framework that has been developed by Rajagopal and Srinivasa [8] to describe the response of bodies with multiple configurations can be used to generate rate type models for blood with shear-thinning behavior, with relaxation times depending on the shear rate and where the viscoelastic character of blood becomes less important with increasing shear rate. Recently Anand and Rajagopal [9] derived a model for blood in the context of a general thermodynamic framework which was shown to be in good agreement with experimental data, in steady Poiseuille and oscillatory flows.

Numerical simulations are certainly considered important tools for prediction of non-Newtonian phenomena, in particular for blood flow models in relevant geometries. Over the past two decades intensive research and significant progress has been made in this area, mainly for steady and unsteady flows of viscoelastic differential and rate-type models (see [10], the monographs [11,12] and references cited therein). The major drawback of many numerical schemes due to the tremendous amount of computation needed and to their inaccuracy or loss of convergence for high values of the Weissenberg number (referred as the “high Weissenberg number problem”) is mainly related to the use of inappropriate boundary conditions and to the hyperbolic nature of the constitutive equations. One of the problems is that a straightforward Galerkin discretization of the constitutive law has poor stability properties if the advection term involving the velocity field and the stress tensor becomes dominant. The other problem is related to the mixed mathematical structure of the nonlinear systems whose behavior under discretization is poorly understood. Typically, specific numerical upwinding or artificial diffusivity techniques must be used, together with appropriate choices of the spaces for velocity, stress and pressure, in such a way that the compatibility LBB inf-sup condition for velocity and pressure fields is satisfied, and the stress has higher accuracy than the velocity. In addition, advanced computational techniques such as highly adaptive refinement, parallel processing and novel matrix solvers will make the computations more affordable. The numerical schemes used for solving these complex systems of PDEs, in particular for our shear-dependent generalized Oldroyd-B model, must be based on a deep understanding of the mixed mathematical structure of the equations (elliptic/hyperbolic in steady case), in order to prevent numerical instabilities on mathematically well-posed problems.

Over the last twenty years, the finite element method has dominated the field of computational rheology. Most of the research was focused on achieving the highest possible Weissenberg number at which numerical stability was still maintained (see [13] for a review of progress in the period 1987–1997). Stabilization techniques such as Streamline Upwind (SU), Streamline Upwind Petrov–Galerkin (SUPG) and their variants have been successfully used by several authors for steady and time dependent flows (see [14–17]) who observed in particular that the increased stability was usually associated with a deterioration in accuracy. To take into account the hyperbolic nature of the constitutive equations, the discontinuous Galerkin (Lesaint–Raviart) method has been also applied to viscoelastic flow computations (see [18–20]) as well as the method of characteristics (or Lagrange–Galerkin method) introduced in [21] and based on [22] for the Navier–Stokes equations.

More recently there has been a renewed interest in the use of finite volume methods to model viscoelastic flow (following the pioneer work of Patankar [23] for Newtonian flows) due to their advantages in terms of computational

resources. These works go back to [24,25] followed by [26–28], among others, who used orthogonal staggered grids to solve flow through the 4:1 planar contraction geometry. In these algorithms pressure and stress unknowns were placed at the center of the control volumes to avoid numerical instabilities related to the singularity at the re-entrant corner. A first order upwind approximation or a semi-Lagrangian method was used for the discretization of the convective terms. However, staggered grids are not well adapted to complex geometries and, to overcome this difficulty, collocated grids have been used by several authors [29–31,26,32] for both structured and unstructured meshes, using higher-order upwind approximations for the convective terms (as in the QUICK, MINMOD and SMART schemes, for example) and SIMPLE-like algorithms to solve the system of equations.

Combined finite element and finite volume (FE/FV) methods have been developed for viscoelastic flows to take advantage of both methods related to the mixed structure of the governing equations. Typically finite elements are applied to the equations of momentum and mass and finite volume schemes are applied to the hyperbolic constitutive equations. In this regard we cite the important contribution of Sato and Richardson [33] and Wapperom and Webster [34], both using a Taylor–Galerkin/pressure-corrected method for time discretization. In [33] the authors used a finite volume cell-centered method for the constitutive equation, whereas a control volume finite element (CVFE) method developed in [29], is used in [34].

Our purpose in this paper is to present a numerical study of steady flows of the generalized Oldroyd-B fluids introduced in [35], using a hybrid FE/FV method based on CVFE with conformal finite elements. This model is able to capture shear-thinning and viscoelastic effects and can be considered thermodynamically based, in the simple case where the relaxation time is supposed to be a constant. Combined effects of inertia, viscoelasticity and viscosity are shown when the method is applied to the numerical simulation of flow in a smooth stenosed channel.

Beginning with this introduction, the paper is organized as follows. The governing equations and appropriate nondimensionalization are introduced in Section 2. In Section 3 we describe in detail the combined FE/FV numerical method applicable both on stuctured and unstructured meshes. Section 4 is devoted to numerical results. We begin with the validation of our methodology on a planar 4:1 contraction benchmark problem for Oldroyd-B creeping flows. This is followed by the numerical study of the shear-thinning and shear-thickening viscosity effects of the generalized Oldroyd-B flows. Finally, the qualitative numerical behavior of the flow through a smooth stenosed channel is also investigated for a range of shear-thinning viscosity parameters. The paper ends with concluding remarks.

We notice that partial occlusion of blood vessels due to stenotic obstruction (lumen area reduction) is one of the most frequent abnormalities of the vascular system. There is strong evidence that fluid dynamical factors play a major role in the development and progression of atherosclerotic plaques and other arterial lesions, leading to vessel stenosis (see [36,37]) but their specific role is not well understood. This work lays the foundation for future applications to pulsatile flows in stenotic two- and three-dimensional vessels, under reliable physiological data.

2. The mathematical model

We consider an incompressible fluid in a bounded domain $\Omega \subset \mathbb{R}^2$ and suppose that the external forces are neglected. The continuity and momentum equations are written as follows:

$$\nabla \cdot \mathbf{u} = 0, \quad (2.1)$$

$$\rho \left(\frac{\partial \mathbf{u}}{\partial t} + \mathbf{u} \cdot \nabla \mathbf{u} \right) = \nabla \cdot \mathbf{T}, \quad (2.2)$$

where \mathbf{u} is the velocity field, $\rho > 0$ the constant density and \mathbf{T} is the Cauchy stress tensor. This tensor is given by $\mathbf{T} = -p\mathbf{I} + \boldsymbol{\sigma}$ where p represents the pressure (a Lagrange multiplier arising from incompressibility) and $\boldsymbol{\sigma}$ is the extra-stress tensor.

Here we consider the extra-stress tensor given by the constitutive equation for a generalized Oldroyd-B fluid,

$$\boldsymbol{\sigma} + \lambda_1 \overset{\nabla}{\boldsymbol{\sigma}} = 2\mu(|D\mathbf{u}|^2)D\mathbf{u} + 2\lambda_2 \overset{\nabla}{D\mathbf{u}}, \quad (2.3)$$

where $\lambda_1, \lambda_2 > 0$ are the viscoelastic constants (relaxation and retardation time, respectively) with $\lambda_1 \geq \lambda_2$ and $\mu : \mathbb{R}^+ \rightarrow \mathbb{R}^+$ is the viscosity function satisfying $\mu(0) > 0$. The symbol (\cdot) denotes the Oldroyd objective derivative

and is defined by

$$\overset{\nabla}{\sigma} = \frac{\partial \sigma}{\partial t} + \mathbf{u} \cdot \nabla \sigma - \sigma (\nabla \mathbf{u})^T - (\nabla \mathbf{u}) \sigma. \quad (2.4)$$

Here $D\mathbf{u} = \frac{1}{2}(\nabla \mathbf{u} + (\nabla \mathbf{u})^T) = \frac{1}{2}(\frac{\partial u_i}{\partial x_j} + \frac{\partial u_j}{\partial x_i})_{i,j=1,2}$ represents the symmetric part of the velocity gradient and is called the rate of deformation tensor.

We decompose the extra-stress tensor σ into the sum of its Newtonian part $\tau_N = 2\frac{\lambda_2}{\lambda_1}D\mathbf{u}$ and its viscoelastic part τ_v . Replacing $\sigma = \tau_N + \tau_v$ by its value in (2.3), we obtain for τ_v the following relation

$$\tau_v + \lambda_1 \overset{\nabla}{\tau}_v = 2 \left(\mu(|D\mathbf{u}|^2) - \frac{\lambda_2}{\lambda_1} \right) D\mathbf{u}. \quad (2.5)$$

Since we look for steady solutions, the continuity and momentum equations can be written as

$$\nabla \cdot \mathbf{u} = 0, \quad (2.6)$$

$$\rho(\mathbf{u} \cdot \nabla \mathbf{u}) = -\nabla p + \nabla \cdot \tau_v + \frac{\lambda_2}{\lambda_1} \Delta \mathbf{u}. \quad (2.7)$$

Here we consider the particular case of the Carreau–Yasuda viscosity function given by

$$\mu(|D\mathbf{u}|^2) = v + v_0(1 + |D\mathbf{u}|^2)^q, \quad (2.8)$$

where q is a real number, v, v_0 are nonnegative real numbers such that $v + v_0 > 0$, related to the bounded asymptotic viscosities $\lim_{|D\mathbf{u}|^2 \rightarrow +\infty} \mu(|D\mathbf{u}|^2) = \mu_\infty$ and $\lim_{|D\mathbf{u}|^2 \rightarrow 0} \mu(|D\mathbf{u}|^2) = \mu_0$. If $q > 0$, this viscosity function is increasing with the shear rate $|D\mathbf{u}|^2$ and the corresponding fluid has a shear-thickening behavior, while $q < 0$ corresponds to a decreasing viscosity function with shear-rate and the fluid is shear-thinning. The classical viscoelastic Oldroyd-B model, with a constant viscosity, is recovered with $q = 0$.

We consider the dimensionless form of the system by introducing the following non-dimensional quantities

$$x = \frac{\tilde{x}}{L}, \quad \mathbf{u} = \frac{\tilde{\mathbf{u}}}{U}, \quad p = \frac{\tilde{p}L}{(v + v_0)U}, \quad \tau = \frac{L\tilde{\tau}_v}{(v + v_0)U}, \quad \lambda_1 = \tilde{\lambda}_1, \quad \lambda_2 = \tilde{\lambda}_2,$$

where the symbol \sim is attached to the dimensional quantities (L represents a reference length and U a characteristic velocity of the flow). We also introduce the Weissenberg number $\mathcal{W}e = \frac{\lambda_1 U}{L}$, the Reynolds number $\mathcal{R}e = \frac{\rho UL}{v + v_0}$, the coefficient $1 - w = \frac{\lambda_2}{\lambda_1(v + v_0)}$ and the viscosity coefficient $\eta = \frac{v_0}{v + v_0}$. Finally, the dimensionless system is formulated as follows

$$\begin{cases} -(1 - w)\Delta \mathbf{u} + \mathcal{R}e \mathbf{u} \cdot \nabla \mathbf{u} + \nabla p = \nabla \cdot \tau & \text{in } \Omega, \\ \nabla \cdot \mathbf{u} = 0 & \text{in } \Omega, \\ \tau + \mathcal{W}e(\mathbf{u} \cdot \nabla \tau - \sigma_1(\nabla \mathbf{u}, \tau)) = 2(w + \eta \sigma_2(|D\mathbf{u}|))D\mathbf{u} & \text{in } \Omega \end{cases} \quad (2.9)$$

where $\sigma_1(\nabla \mathbf{u}, \tau) = \tau(\nabla \mathbf{u})^T + (\nabla \mathbf{u})\tau$ and $\sigma_2(x) = (1 + x^2)^q - 1$.

This formulation is not suitable for dealing with finite volume techniques and therefore we rewrite system (2.9) in divergence form. It becomes

$$\begin{cases} -(1 - w)\Delta \mathbf{u} + \mathcal{R}e \mathbf{u} \cdot \nabla \mathbf{u} + \nabla p = \nabla \cdot \tau & \text{in } \Omega, \\ \nabla \cdot \mathbf{u} = 0 & \text{in } \Omega, \\ \tau + \mathcal{W}e \operatorname{div}(\tau \otimes \mathbf{u}) = \mathcal{W}e \sigma_1(\nabla \mathbf{u}, \tau) + 2(w + \eta \sigma_2(|D\mathbf{u}|))D\mathbf{u} & \text{in } \Omega \end{cases} \quad (2.10)$$

where \otimes is the dyadic product.¹ This system is closed with appropriate boundary conditions that depend on the flow geometry and will be specified in the next sections. Here and in what follows, vector and tensor fields will be denoted by boldface letters.

¹ Using the Einstein summation convention: $\operatorname{div}(\tau \otimes \mathbf{u})_{ij} = \tau_{ij} \frac{\partial u_k}{\partial x_k} + u_k \frac{\partial \tau_{ij}}{\partial x_k}$.

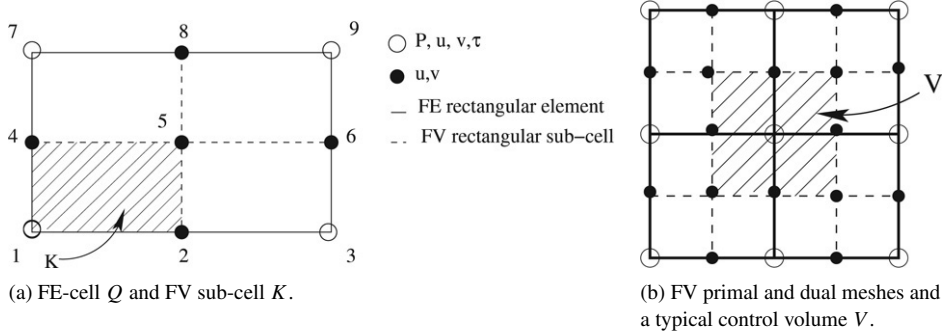


Fig. 1. Hybrid FE/FV spatial discretization.

3. Numerical method

Problem (2.10) is a coupled system of partial differential equations of mixed elliptic-hyperbolic type on the three unknowns (u, p, τ) . This requires an appropriate decoupling numerical technique to take advantage of the mixed mathematical structure of the system and to avoid the excessive computer memory requested when a coupled solution technique is implemented. The current hybrid spatial discretization combines a finite element discretization (Taylor–Hood method) for continuity and momentum equations, to obtain an approximation of the velocity components-pressure (u, p) , with a cell-vertex finite volume scheme for the constitutive equation (2.10)₃ to obtain an approximation of the viscoelastic stress tensor. The uncoupling between the two sets of nonlinear discretized equations is achieved by means of a Picard’s iterative scheme. In order to describe the hybrid finite element–finite volume (FE–FV) method, we need to construct the computational mesh and describe the discretization method and numerical algorithm.

3.1. Computational mesh and discretization

Let $\Omega \subset \mathbb{R}^2$ be the computational domain and, for each $h > 0$ let $(\mathcal{Q}_h)_h$ be a regular family of quadrangles, with sides parallel to the coordinate axes of a cartesian frame, covering $\bar{\Omega}$. For each integer $k \in \mathbb{N}$, \mathbb{Q}_k denotes the space of all polynomials, defined in \mathbb{R}^2 , of degree less or equal to k with respect to each variable.

The finite element discretization adopted here is based on piecewise continuous $\mathbb{Q}_2 - \mathbb{Q}_1$ Taylor–Hood elements for the approximation of the pair velocity components-pressure (as indicated in Fig. 1(a)). This is a well documented FE method (see e.g. [38,39]) where the velocity–pressure interpolation satisfies the usual compatibility condition (known as the Ladyzhenskaya–Babuška–Brezzi (LBB) condition) between the function spaces for velocity and pressure that prevents locking and spurious oscillation phenomena. The nonlinear convective term of the Navier–Stokes equations is discretized as $\mathbf{u}^{k-1} \cdot \nabla \mathbf{u}^k$ where the superscript $k - 1$ indicates the value taken at the previous iteration and k is the current iteration of Picard’s method.

The basic idea of the finite volume method applied to the discretization of the viscoelastic stress tensor is to integrate the constitutive equation (2.10)₃ over a control volume (of triangles or quadrangles) and to use Gauss’ divergence theorem to compute a boundary integral, whenever possible. Two different mesh strategies can be adopted to locate the approximate values of the unknowns. The first one is a cell-centered finite volume method where all components of the stress tensor are taken at the center of the mesh cells [26,23,25]. This approach represents a good approximation of the unknown over the volume in every case. However, the disadvantage of such a choice is that the fluxes on the interfaces of the control volumes are not well approximated in the case of unstructured meshes. Further interpolations are required to recover the FE nodal stress values to include in the momentum equation (2.10)₁ (as for the pressure, a piecewise continuous \mathbb{Q}_1 function is needed to approximate the stress in order to avoid spurious oscillation phenomena [40]). To overcome these difficulties, a second strategy can be applied. The method consists in meshing the computational domain with quadrangles (or triangles, see Remark 1 below) and locating the stress unknowns at the vertices of the mesh cells. Then a control volume is constructed around each vertex in order to obtain a dual mesh (see below for a more detailed description). This method is known as the cell vertex FV method [41–43] and is the one adopted in this paper. It can be compared to a low order FE method, it is better adapted to recover the

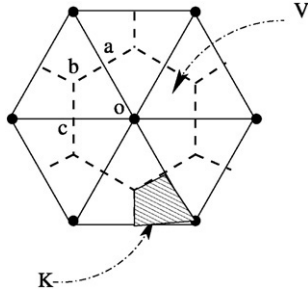


Fig. 2. Typical Control Volume V (dashed line) and subvolume K (filled volume) on an unstructured mesh.

FE nodal stress unknown and to complex geometries and it allows for an element-by-element assembling matrix as in the FE method.

The finite volume method applied to the discretization of the stress in (2.10)₃ uses the finite element mesh as a platform or *primal* mesh. For each quadrangle $Q \in (\mathcal{Q}_h)_h$, we take its gravity center (intersection of the median lines) and join it to the midpoint of each edge, dividing Q into four equal subquadrangles. We obtain a new regular family of quadrangles denoted by $(K_h)_h$. An element $K \in (K_h)_h$ has nodes 1-2-4-5, for example (see Fig. 1(a)). This new family is used to generate the *dual* mesh denoted by $(V_h)_h$ and composed of control volumes V : for each vertex of a quadrangle Q , V is the union of the four FV sub-cells containing this vertex. Fig. 1(b) is an illustration of the FV-primal and dual meshes constructed on a rectangular domain Ω .

Remark 1. The hybrid FE–FV method can be applied to a triangular mesh in a straightforward way. In that case, the domain $\bar{\Omega}$ is covered with a regular family of triangles $(K_h)_h$ and the pair velocity components-pressure is approximated by piecewise continuous $\mathbb{P}_2^+ - \mathbb{P}_1$ elements (\mathbb{P}_k , $k \geq 0$ is the space of polynomials of degree less or equal to k and the superscript + indicates a bubble function added to the polynomial space). The stress unknowns are located at the vertices of each triangle and are taken constant in each control volume. A control volume is the union of subvolumes sharing the same vertex. Each subvolume is obtained by connecting the gravity center of the triangle to each midside (see Fig. 2).

In what follows the discretization method will be described in such a way that both the quadrangular or triangular meshes can be considered.

Next, we introduce the discretization of the constitutive equation by the finite volume method. Let φ^i be the basis functions associated to the vertex i . Each component of the stress tensor τ can be written in this basis as

$$\Phi_h = \sum_{i=1}^{\text{nbf}} \Phi_h^i \varphi^i \quad (3.1)$$

where Φ_h^i is the value of Φ_h on the vertex i . The variable Φ is a common notation representing τ_{xx} , τ_{xy} and τ_{yy} , components of the stress tensor τ . The number nbf indicates the number of basis functions, here nbf = 4 (nbf = 3, in the case of a triangular mesh).

Let V be a control volume belonging to $(V_h)_h$. Integrating on V the constitutive equation (2.10)₃ and using Gauss' theorem we get

$$\int_V \tau dx + \mathcal{W}e \int_{\partial V} \tau u \cdot \vec{n} d\sigma = \mathcal{W}e \int_V (\tau(\nabla u)^T + (\nabla u)\tau) dx + \int_V (w + \eta\sigma_2(|Du|)) (\nabla u + (\nabla u)^T) dx \quad (3.2)$$

where \vec{n} denotes the unit outward normal on the boundary. In order to compute the integrals, we use a function that maps a current element Q into a reference element \hat{Q} . As in finite element methods, we restrict ourselves to convex quadrangles. Usually, the Jacobian matrix is non constant and depends on the coordinate system. Therefore, the equality

$$\forall Q \in (\mathcal{Q}_h)_h, \quad \int_Q dx = |D\hat{F}_Q| \text{mes}(\hat{Q}),$$

where $\hat{\mathbf{F}}_Q$ is a mapping from \hat{Q} to Q and $D\hat{\mathbf{F}}_Q$ is its Jacobian matrix is not verified. However, this property is a simple way to guaranty the mass balance on the common edge between two volumes. It is simply recovered if we suppose that the Jacobian matrix is constant all over the element Q . So we take $D\hat{\mathbf{F}}_Q = D\hat{\mathbf{F}}_Q(c^*)$ where c^* is the center of the volume Q . This kind of approximation is used when there are physical coefficients in the equation. This approach is strongly recommended as emphasized by Patankar [23].

Remark 2. In the case of a triangular mesh, the mapping is affine and thus its Jacobian matrix is constant.

Now, using the fact that $V = \bigcup_{K \subset V} K$ or $\partial V = \bigcup_{K \subset V} \partial K$, we discretize Eq. (3.2) by a finite element technique. The convective terms $\int_{\partial V} \boldsymbol{\tau} \mathbf{u} \cdot \vec{n} d\sigma$ appearing in Eq. (3.2) need special attention. The other terms in Eq. (3.2) can be easily integrated by using the midpoint numerical integration rule. So we can write:

$$\int_V \boldsymbol{\tau} dx \sim \boldsymbol{\tau}_V \text{mes}(V) = \boldsymbol{\tau}_V \sum_{K \subset V} \text{mes}(K), \quad (3.3)$$

$$\begin{aligned} \int_V (\boldsymbol{\tau}(\nabla \mathbf{u})^T + (\nabla \mathbf{u})\boldsymbol{\tau}) dx &\sim (\boldsymbol{\tau}(\nabla \mathbf{u})^T + (\nabla \mathbf{u})\boldsymbol{\tau})_V \text{mes}(V) \\ &= (\boldsymbol{\tau}(\nabla \mathbf{u})^T + (\nabla \mathbf{u})\boldsymbol{\tau})_V \sum_{K \subset V} \text{mes}(K), \end{aligned} \quad (3.4)$$

$$\begin{aligned} \int_V (w + \eta \sigma_2(|D\mathbf{u}|)) ((\nabla \mathbf{u})^T + \nabla \mathbf{u}) dx &\sim (w + \eta \sigma_2(|D\mathbf{u}|))_V ((\nabla \mathbf{u})^T + \nabla \mathbf{u})_V \text{mes}(V) \\ &= (w + \eta \sigma_2(|D\mathbf{u}|))_V ((\nabla \mathbf{u})^T + \nabla \mathbf{u})_V \sum_{K \subset V} \text{mes}(K), \end{aligned} \quad (3.5)$$

where the subscript V means that the value is taken in the center of the control volume.

As for the convective terms, we first write

$$\int_{\partial V} \boldsymbol{\tau} \mathbf{u} \cdot \vec{n} d\sigma = \sum_{K \subset V} \int_{\partial K} \boldsymbol{\tau} \mathbf{u} \cdot \vec{n} d\sigma = \sum_{K \subset V} \mathbf{g}(\boldsymbol{\tau}, \mathbf{u}_V, \mathbf{u}_{V'}, \vec{n}_\Gamma),$$

where \mathbf{g} is the numerical flux and V and V' are two volumes sharing the edge Γ . The flux on γ is discretized using an upwind scheme as follows

$$\boldsymbol{\tau}^{up} \int_\Gamma \mathbf{u} \cdot \vec{n} d\sigma = \begin{cases} \boldsymbol{\tau}_V (\mathbf{u} \cdot \vec{n})_\Gamma & \text{if } (\mathbf{u} \cdot \vec{n})_\Gamma > 0, \\ \boldsymbol{\tau}_{V'} (\mathbf{u} \cdot \vec{n})_\Gamma & \text{otherwise} \end{cases} \quad (3.6)$$

and similarly for the other common edges between two volumes.

This scheme is unconditionally stable and insures that the solution remains bounded (this means that the value of the computed node stays between the range of values defined by its neighbours). Unfortunately, this scheme is very dissipative and is of first order if the flux is not parallel to the axis, in the case of a quadrangular mesh, or oblique in the case of a triangular mesh. Therefore, refined meshes are necessary to obtain a “good” solution. The definition of “good” depends on the problem to be solved and the goal to be reached. In most cases, this scheme is good enough. Ongoing research is devoted to the construction of less dissipative and more accurate schemes but no satisfactory solutions have been found for dimensions higher than one. The most common scheme used is the QUICK scheme with deferred-correction approach where the lower order term (which is the term arising in the upwind scheme) is taken implicitly and the higher order terms are treated explicitly. This construction is a requirement, otherwise negative values appear on the diagonal of the matrix which leads to an unrealistic solution or to the divergence of the scheme [26]).

We also point out that the velocity field in Eq. (2.10)₃ must be constant on each control volume. More precisely, the velocity field as well as the stress components need to have a bilinear (\mathbb{Q}_1 function) representation on the primal mesh. Since, the velocity field is biquadratic on this mesh, we construct an interpolation of the velocity field in the following way. Each component of the velocity has nine degrees of freedom on each element (see Fig. 1) and we remark that, on each side of the dual volume, the velocity component has two degrees of freedom. Since the finite volume method deals with low degree polynomials ($\mathbb{P}_0, \mathbb{P}_1, \mathbb{Q}_0$ or \mathbb{Q}_1), we can interpolate the velocity field using \mathbb{Q}_1 polynomials on each subquadrangle. This is equivalent to the so-called finite element $\mathbb{Q}_2iso\mathbb{Q}_1$.

Remark 3. The interpolation of the velocity components is done in a similar way in triangular or quadrangular meshes. Each triangle is divided into six subtriangles by connecting the gravity center to both the vertex or the middle-edge (for example, the triangle formed by the points o-b-a, see Fig. 2 for the notations). On each subtriangle, the velocity components are interpolated with continuous piecewise linear functions (\mathbb{P}_1).

Let us briefly describe the numerical algorithm. We use Picard's iterations to reduce the nonlinear problem to a sequence of linear solvers.

- (1) Initialize variables.
- (2) Solve the continuity and momentum equations (Stokes/Navier–Stokes) for (\mathbf{u}, p) .
- (3) Solve the constitutive equation for the stress $\boldsymbol{\tau}$.
- (4) Relax the stress unknowns.
- (5) Go to 2 and repeat until convergence.

The Bi-Conjugate Gradient Stabilized (BiCGStab) solver (see [44]) has been applied to the inner iterations with a tolerance equal to 10^{-10} . The Picard's iterations were stopped if $\frac{\|\Phi^{k+1} - \Phi^k\|_2}{\|\Phi^{k+1}\|_2} \leq 10^{-8}$ ($\|\cdot\|_2$ is the L^2 discrete norm), where Φ^{k+1} denotes the most recent approximation of the unknown from the outer iteration and Φ^k is the preceding approximation.

4. Numerical results

We proceed with the validation of our FE/FV hybrid method on the classical Oldroyd-B fluid, assuming creeping flow, i.e. $Re = 0$, as a starting point. The method is applied to a standard benchmark: flow through an abrupt planar four-to-one (4:1) contraction, for a range of Weissenberg numbers up to $We = 3$. The same benchmark problem is used to highlight the shear-thinning and shear-thickening viscosity effects on the flow, when the full generalized Oldroyd-B model (2.10) is considered. Finally the method is also applied to generalized Oldroyd-B flows in a smooth stenosed channel. Preliminary results are presented showing in particular the influence of the viscoelastic, inertial and shear-thinning effects on the qualitative behavior of the flow.

4.1. Validation of the numerical method

We consider the flow of an Oldroyd-B fluid through an abruptly contracting channel in which the ratio of the channel widths before and after the contraction is 4:1. A schematic diagram of the upper half of this geometry is shown in Fig. 3. The governing equations are given by:

$$\begin{cases} -(1-w)\Delta\mathbf{u} + \nabla p = \nabla \cdot \boldsymbol{\tau} & \text{in } \Omega, \\ \nabla \cdot \mathbf{u} = 0 & \text{in } \Omega, \\ \boldsymbol{\tau} + We\operatorname{div}(\boldsymbol{\tau} \otimes \mathbf{u}) = We \left(\boldsymbol{\tau}(\nabla \mathbf{u})^\top + (\nabla \mathbf{u})\boldsymbol{\tau} \right) + 2wD\mathbf{u} & \text{in } \Omega \end{cases} \quad (4.1)$$

which is the inertialess form of (2.10) with constant viscosity. In order to close the system of PDE's we need to impose suitable boundary conditions. At the inlet we prescribe a Poiseuille velocity profile and, due to memory effects of viscoelastic fluids, all components of the viscoelastic extra-stress must also be prescribed. Moreover, we assume that the downstream exit length is chosen long enough so that at the outlet a fully developed Poiseuille flow is also prescribed. No-slip conditions are imposed on Γ_{wall} and symmetry conditions are specified on the axis of symmetry. More precisely, from the fully developed profiles, the prescribed values can be obtained analytically (see [32]), and these Dirichlet boundary conditions are given by

Inlet section (Γ_{in}):

$$\begin{aligned} u(-L_{\text{in}}, y) &= \frac{1}{128}(16 - y^2), & v(-L_m, y) &= 0 \quad (\text{with } \mathbf{u} = (u, v)) \\ \tau_{xx}(-L_{\text{in}}, y) &= \frac{1}{2048}wWe y^2, \\ \tau_{xy}(-L_{\text{in}}, y) &= -\frac{w}{64}y, \\ \tau_{yy}(-L_{\text{in}}, y) &= 0. \end{aligned}$$

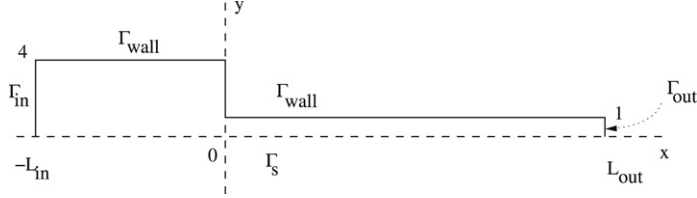
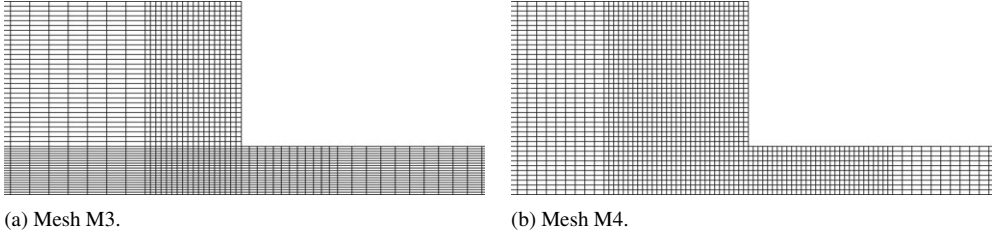
Fig. 3. The 4:1 abrupt planar contraction ($L_{in} = 10$ and $L_{out} = 20$).

Fig. 4. Region around the re-entrant corner.

Outlet section (Γ_{out}):

$$u(-L_{out}, y) = \frac{1}{2}(1 - y^2), \quad v(-L_{out}, y) = 0.$$

Symmetry axis (Γ_s):

$$\frac{\partial u}{\partial y}(x, 0) = v(x, 0) = \tau_{xy}(x, 0) = 0.$$

Wall section (Γ_{wall}):

$$u = v = 0.$$

The 4:1 contraction benchmark problem has been extensively studied (see e.g. [41,27,45,28,46]). It is a numerically challenging and important test problem, in terms of stability at high Weissenberg numbers. Its main difficulty, compared with other benchmarks in smooth geometries, such as the falling sphere in a tube or the flow along an array of cylinders (see e.g. [31,29,47] and references therein), is to catch correctly the singularity at the re-entrant corner. This is the cause of failure of many numerical methods, due to the large stresses developed in this region. A fine mesh around the corner needs to be used to capture the singularity. However, the use of fine meshes reduces the order of the critical Weissenberg number for which the method fails to converge. Another challenging feature of this benchmark problem is to predict the form and behavior of the lip-vortex appearing in the salient corner as a function of the Weissenberg number. We refer to [32] for a review of previous numerical work.

Four different meshes named M1, M2, M3, M4 are considered in this study. M1 is a uniform mesh with a discretization step $h = \frac{1}{5}$ in each direction. M2 is an anisotropic mesh with an area 2×10^{-2} near the corner. Meshes M3 and M4, presented in Fig. 4, are refinements of meshes M2 and M1 respectively. For these meshes, the areas around the re-entrant corner are 5.5×10^{-3} and 10^{-2} , respectively. The dimensionless units U and L are chosen to be $U = \frac{1}{3}$ and $L = 1$, so that $We = \frac{\lambda_1}{3}$. The parameter w is taken equal to $\frac{8}{9}$ for comparison with other results in the literature.

Fig. 5 presents, for the four different meshes, the stress tensor components evolution along the line $y = 1$, which crosses the re-entrant corner. The Weissenberg number retained here is equal to $We = 1.5$. As expected, a peak appears at the re-entrant corner. Furthermore, the height of the peak depends on the area around the corner: the smaller the area, the higher is the peak (this can be detected when results on the coarser meshes M1 and M2 are compared with those on the finer meshes M3 and M4). We remark that for the first component of the stress tensor τ_{xx} (Fig. 5(a)) a gap appears between the profiles obtained using mesh M1 and the others. This gap does not appear on the profiles of the other components of the stress tensor (Fig. 5(b) and (c)). This is essentially due to the parabolic profile of the first

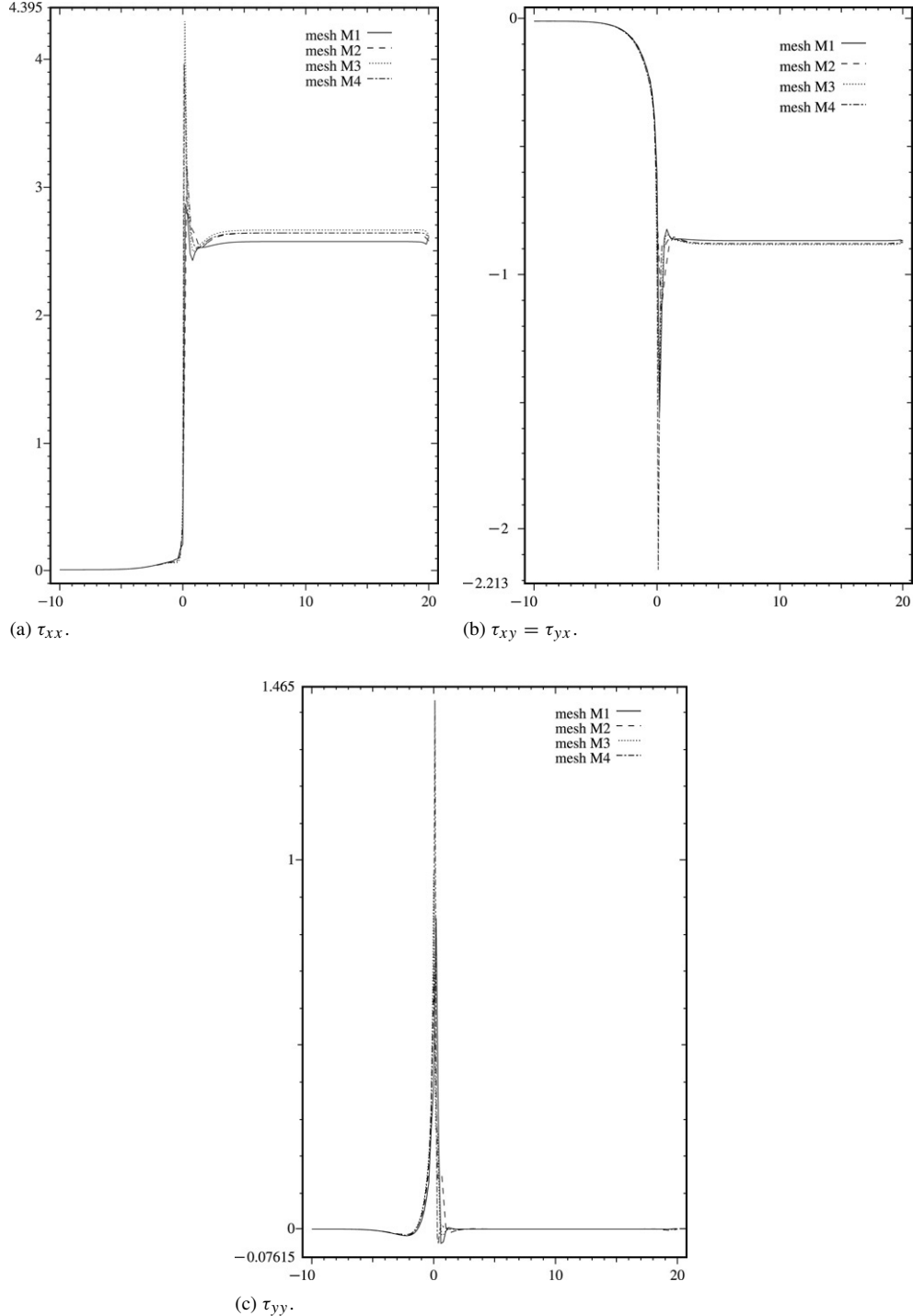


Fig. 5. Evolution of the stress tensor τ along the line $y = 1$ on the 4:1 contraction geometry, for different meshes, with Weissenberg number $\mathcal{W}e = 1.5$.

component of the stress tensor in a channel and to the poor refinement of mesh M1, in the y direction compared to the other meshes. The second and third components of the stress tensor have linear profiles, which are better approached in the different meshes. A refinement of the narrow channel permits reduction of this gap.

Fig. 6 illustrates the evolution of the second and third components of the stress tensor on mesh M4. As we can see, the curves are quasi identical in the two channels (upstream and downstream of the re-entrant corner) and are independent of the Weissenberg number, which is an expected result (see e.g. [27,46]). As for τ_{xx} we observe that the profiles depend on the Weissenberg number, with a negative peak value for the Newtonian flow ($We = 0$). The only relevant difference between these curves is at the re-entrant corner, since the peak is more important when the Weissenberg number increases.

Fig. 7 displays the pressure, the stress and the streamline contours for $We = 3$, which is the maximum value of the Weissenberg number achieved in our computations. This figure shows in particular that stress boundary layers develop downstream of the re-entrant corner and attain the highest intensity for $We = 3$. An interesting feature observed also by other authors (see e.g. [32,45,28]) is that the qualitative behavior of the numerical results does not change with the Weissenberg number. On the other hand, we observe that the lip-vortex appears for $We = 3$, using mesh M4 (see **Fig. 7(f)**). The lip-vortex was not detected for smaller values of Weissenberg number on this mesh or on the less refined meshes M1, M2, M3, which suggests that the lip-vortex is attached to fluid viscoelasticity and to mesh size. The results obtained with our FE/FV numerical method are in qualitative agreement with the results of [27,32,45,28], where similar simulation assumptions were considered.

4.2. Effects of non-Newtonian viscosity

Having validated our numerical scheme in the previous section, for an Oldroyd-B creeping flow, we are going to highlight the influence of the shear-thinning and shear thickening effects of non-Newtonian viscosity on the flow of the generalized Oldroyd-B fluid with governing equations expressed by (2.10). This study uses the Carreau–Yasuda viscosity function given by (2.8). All the following results have been obtained in the same framework of the previous section using mesh M4, with $Re = 0$ and with $We = 1$ (*i.e.* relaxation time $\lambda_1 = 3$), for different values of the dimensionless viscosity coefficient η and the power index q .

The evolution of the extra-stress components along the line $y = 1$, crossing the re-entrant corner, is observed in **Figs. 8 and 9**.

Fig. 8 is concerned with shear-thickening fluids ($q \geq 0$). The value $q = 0$ corresponds to the classical Oldroyd-B solution, with a constant viscosity, and is taken as a reference. We recall that the viscoelastic and the viscosity effects of the generalized Oldroyd-B fluids combine the characteristics of both generalized Newtonian and Oldroyd-B fluids, which is clear from the analysis of the plots of **Fig. 8**. We observe that the maximum absolute values of the peaks presented by the stress components at the re-entrant corner are highly influenced by the power index q , increasing with it, for $q < 2$ (**Fig. 8(a), (c) and (d)**) and decreasing when $q = 2$ (**Fig. 8(b)**). **Fig. 8(a)** and (b) show also that the peak with negative values vanishes for q close to 2. Upstream of the re-entrant corner, the quantitative behavior of all components of the stress on the upper boundary of the narrow channel, does not change with q . However downstream of the corner this behavior changes dramatically except for component τ_{yy} where the plots corresponding to different values of q look superposed.

Results for the shear-thinning viscosity ($q \leq 0$) are presented in **Fig. 9**. The behavior of the $\tau_{xy} = \tau_{yx}$ stress components on the upper wall of the narrow channel is the opposite to the one corresponding to the shear-thickening viscosity: increasing maximum values of the stress are associated with decreasing values of q . Moreover, as for the shear-thickening viscosity, the τ_{yy} stress component is not influenced by the power index viscosity, except at the corner, where the maximum value of the peak decreases when q decreases (see **Fig. 9(c)**). As for the τ_{xx} stress component we notice that contrary to the shear-thickening case, the peak does not present any negative values and decreases continuously with q (see **Fig. 9(d)**).

Finally, we point out that some simulations have also been performed for different values of the viscosity parameter η . Results are similar to those obtained with $\eta = \frac{1}{2}$ and are not reported here. However, all the simulations failed for a power index higher than $q = 2$, independently of the value of η and for different Weissenberg numbers.

4.3. Flow in a stenosed channel

Numerical simulations have also been performed in a smooth stenosed channel, in view of their application to blood flow in small size vessels, as already mentioned in the introduction.

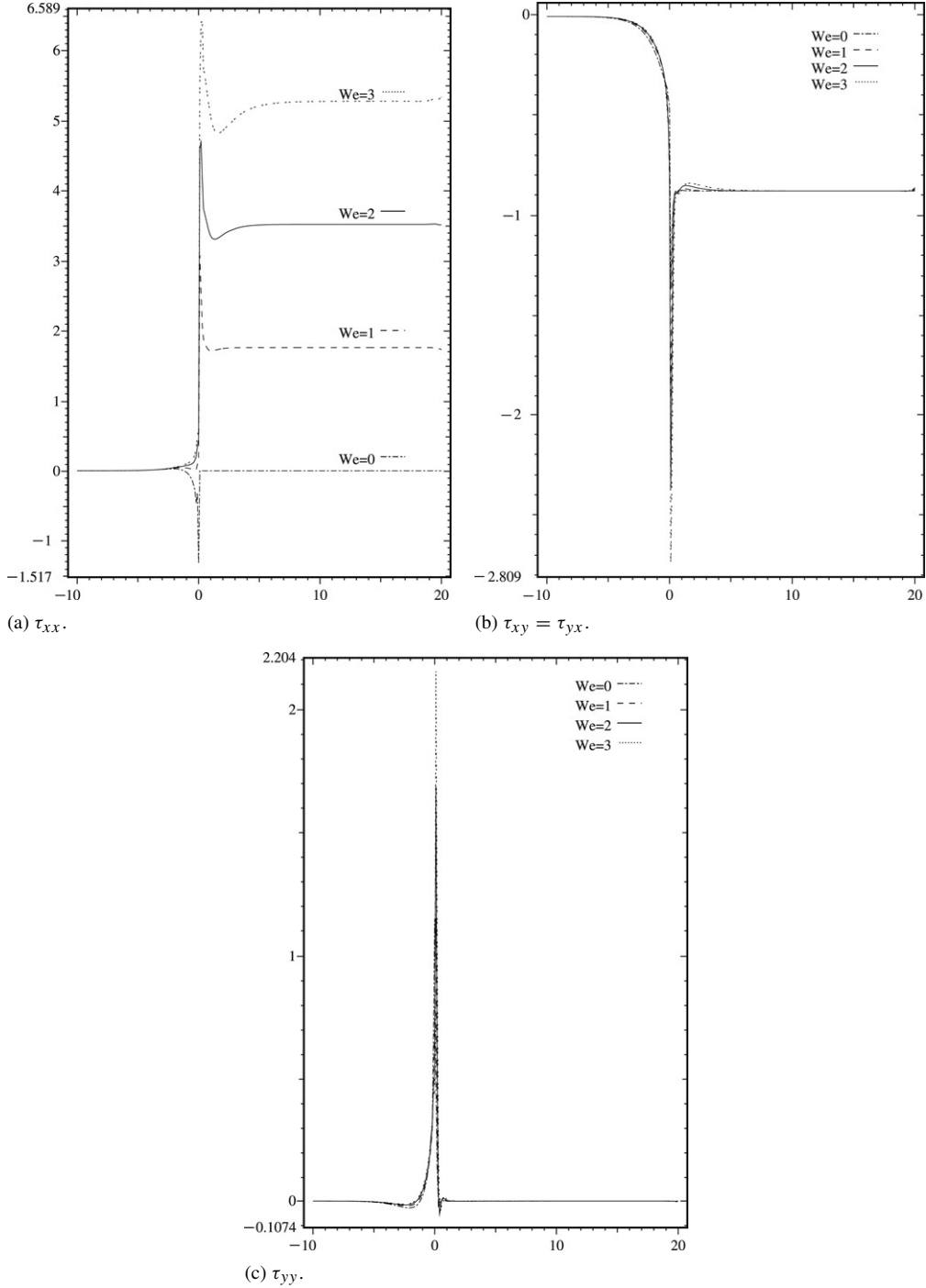


Fig. 6. Evolution of the stress tensor τ along the line $y = 1$ on the 4:1 contraction, for different Weissenberg numbers ($We = 0, 1, 2, 3$) using mesh M4.

A representative geometry of the stenosis considered in this investigation is shown in Fig. 10, along with all relevant dimensions. The rigid and impermeable lateral wall is modeled as a smooth constriction, given by the equations

$$\text{for } i = 1, 2, \quad f_i(x) = \begin{cases} (-1)^{i+1} R_0 + (-1)^i \frac{h_i}{2} \left(1 + \cos\left(\frac{\pi}{L} x\right)\right), & \text{if } |x| \leq L \\ (-1)^{i+1} R_0, & \text{otherwise.} \end{cases} \quad (4.2)$$

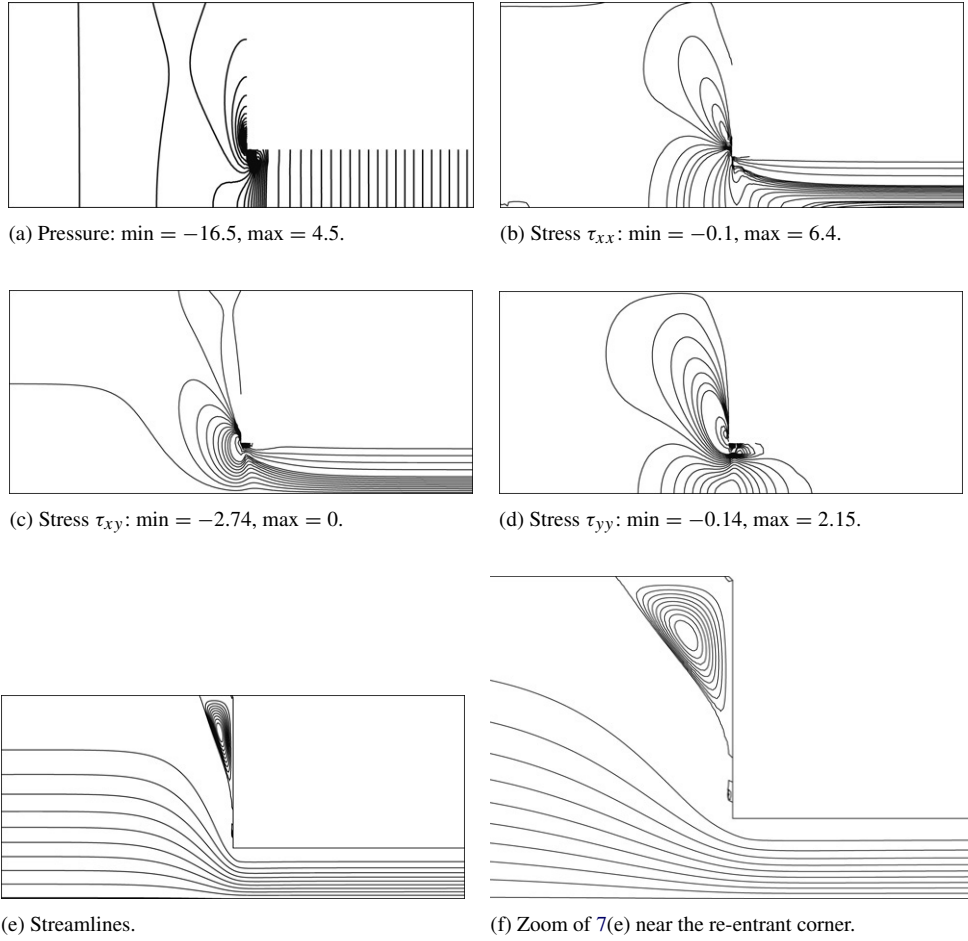


Fig. 7. Pressure, stress and streamline countour lines on the 4:1 contraction, on mesh M4, with Weissenberg number $\mathcal{W}e = 3$.

The indexes 1 and 2 refer to the upper and lower walls, respectively, h_1 and h_2 represent the heights of the stenosis profile, R_0 is the radius of the channel and $L = 2R_0$ is the length of the stenosis profile.

In steady flow simulations long outflow tubes have to be chosen to avoid the influence of outflow boundary conditions on the flow patterns in the stenotic region. Here the channel is $30R_0$ long and we take $R_0 = 1$ and $h_1 = h_2 = 0.3$. These values imply a stenosis with a 30% area reduction, which corresponds to the case of a relatively mild occlusion, leading to local small increasing Reynolds and Weissenberg numbers. Fully developed Poiseuille flows obtained analytically are prescribed upstream and downstream of the stenosis, as Dirichlet boundary conditions, and read as follows

Inlet section (Γ_{in}):

$$\begin{aligned} u(-10R_0, y) &= \frac{1}{2}(1 - y^2), & v(-10R_0, y) &= 0 \\ \tau_{xx}(-10R_0, y) &= 2w\mathcal{W}ey^2, \\ \tau_{xy}(-10R_0, y) &= -wy, \\ \tau_{yy}(-10R_0, y) &= 0. \end{aligned}$$

Outlet section (Γ_{out}):

$$u(20R_0, y) = \frac{1}{2}(1 - y^2), \quad v(20R_0, y) = 0.$$

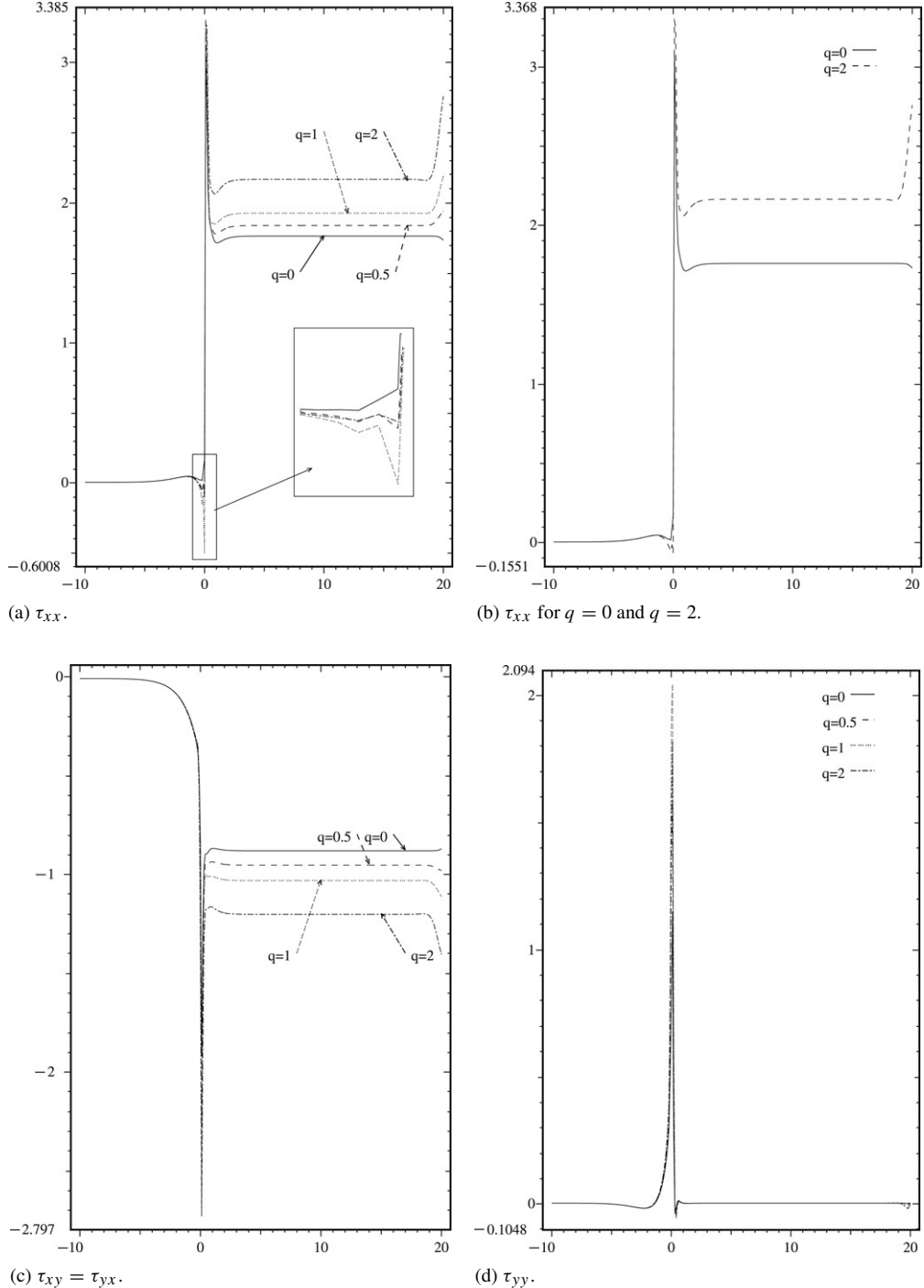


Fig. 8. Evolution of the stress tensor τ along the line $y = 1$ on the 4:1 contraction, with Weissenberg number $We = 1$, viscosity coefficient $\eta = 0.5$ and different values of the power index $q \geq 0$.

Wall section (Γ_{wall}):

$$u = v = 0.$$

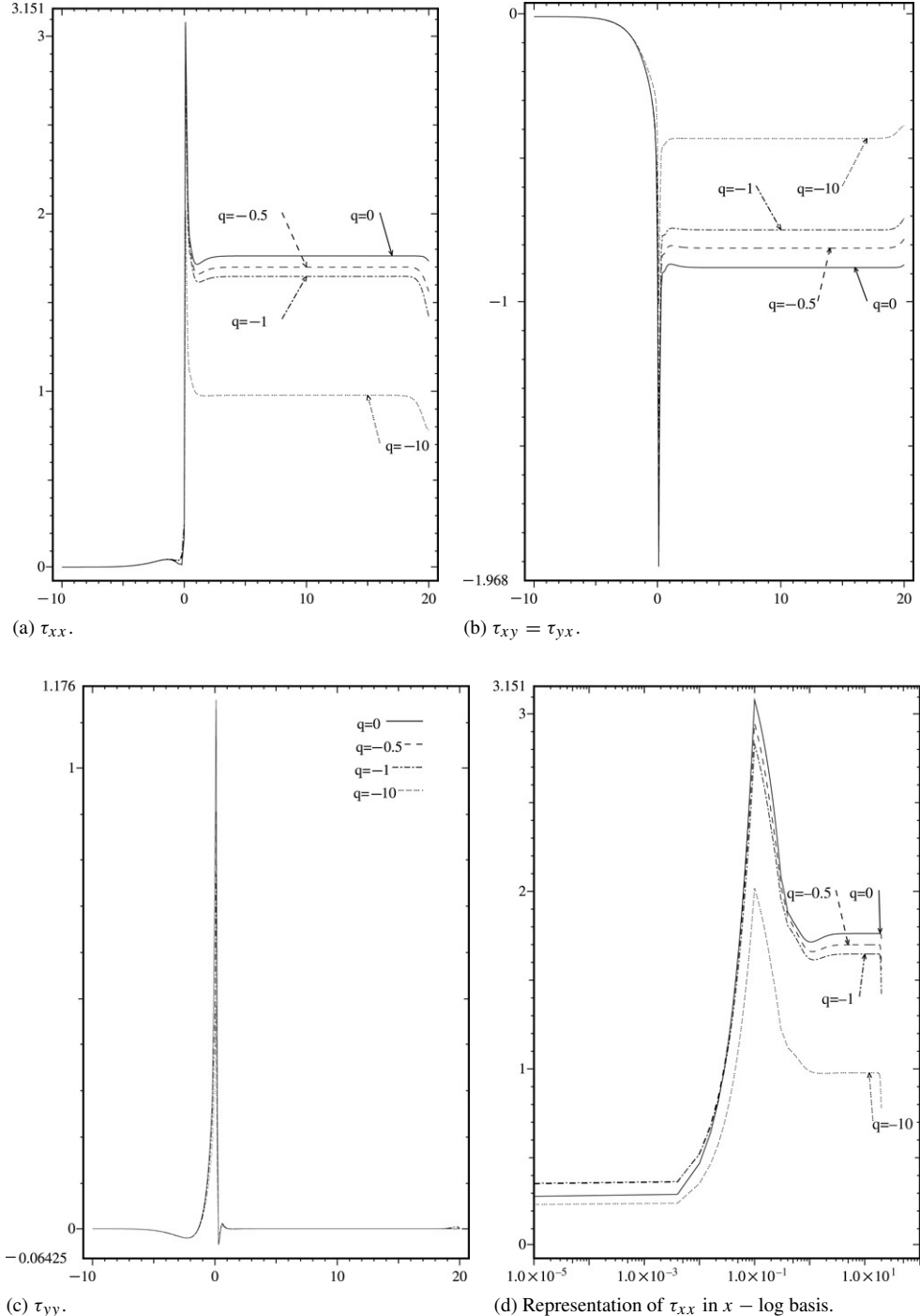


Fig. 9. Evolution of the stress tensor τ along the line $y = 1$ on the 4:1 contraction, with Weissenberg number $We = 1$, viscosity coefficient $\eta = 0.5$ and different values of the power index $q \leq 0$.

Among the hemodynamic parameters of physiological relevance to quantify the progression of arterial diseases related to vessel constriction, is the wall shear-stress (WSS) which measures the force tangential to the vascular wall and can be defined relative to the Cauchy stress tensor T , by

$$\tau_w = -(T \cdot v) \cdot \lambda|_{(f_i(x))_{i=1,2}} \quad (4.3)$$

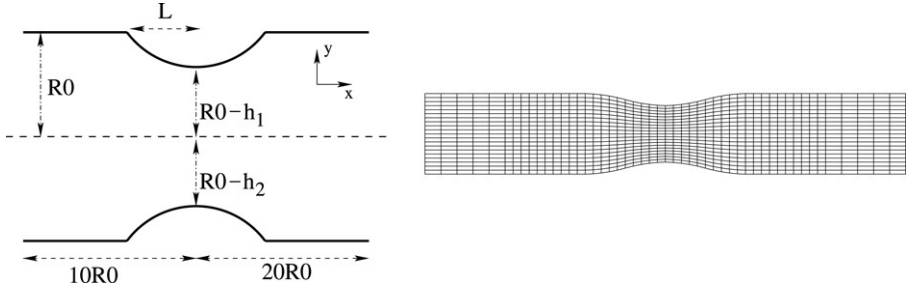


Fig. 10. Geometry and mesh of the stenosed channel.

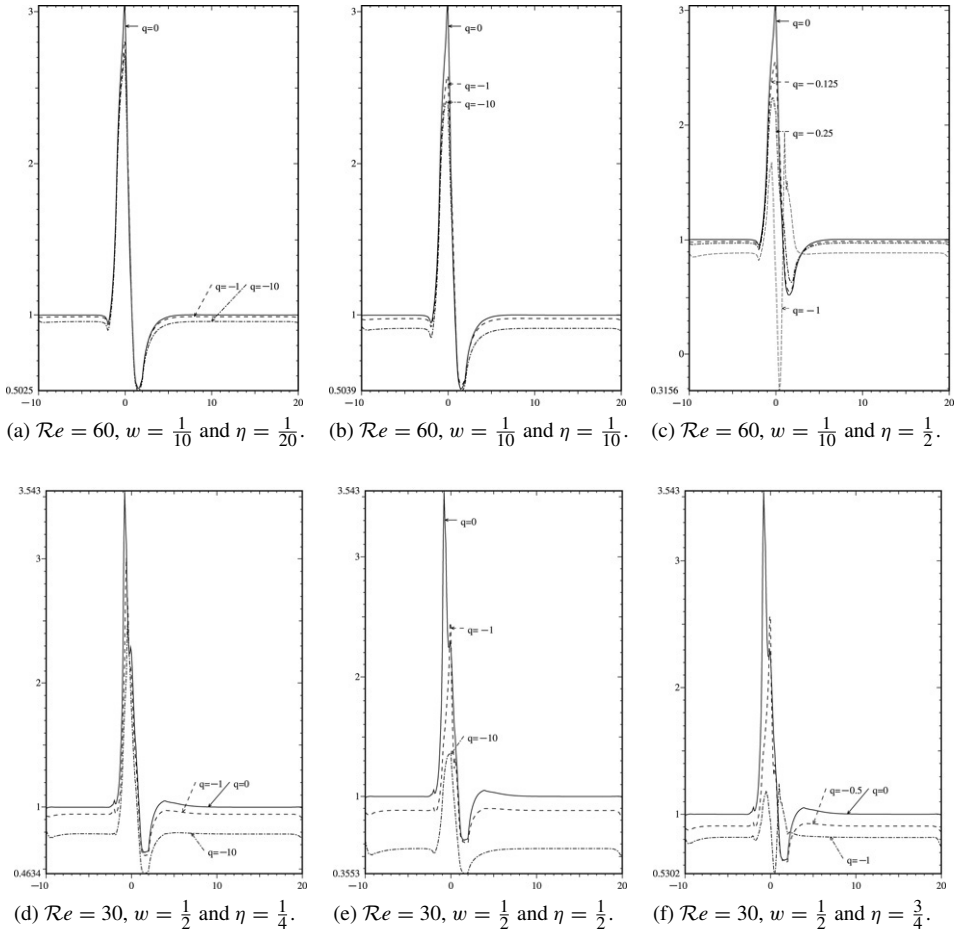


Fig. 11. Evolution of the wall shear stress (WSS) distribution on the upper wall of the stenosis, for different values of the nondimensional parameters.

where ν denotes the unit outward normal and λ is the unit tangent to the wall. Abnormally large values of this quantity are related to a possible rupture of stenotic plaques.

The numerical simulations have been obtained for fixed Weissenberg number $We = 3$, for Reynolds numbers $Re = 30$ and $Re = 60$, relaxation ratios $w = \frac{1}{10}$ and $w = \frac{1}{2}$ (physiological value, see [7]) and for different values of the power ratio η and the power index q , in order to study the shear-thinning viscosity effects of the flow on this geometry.

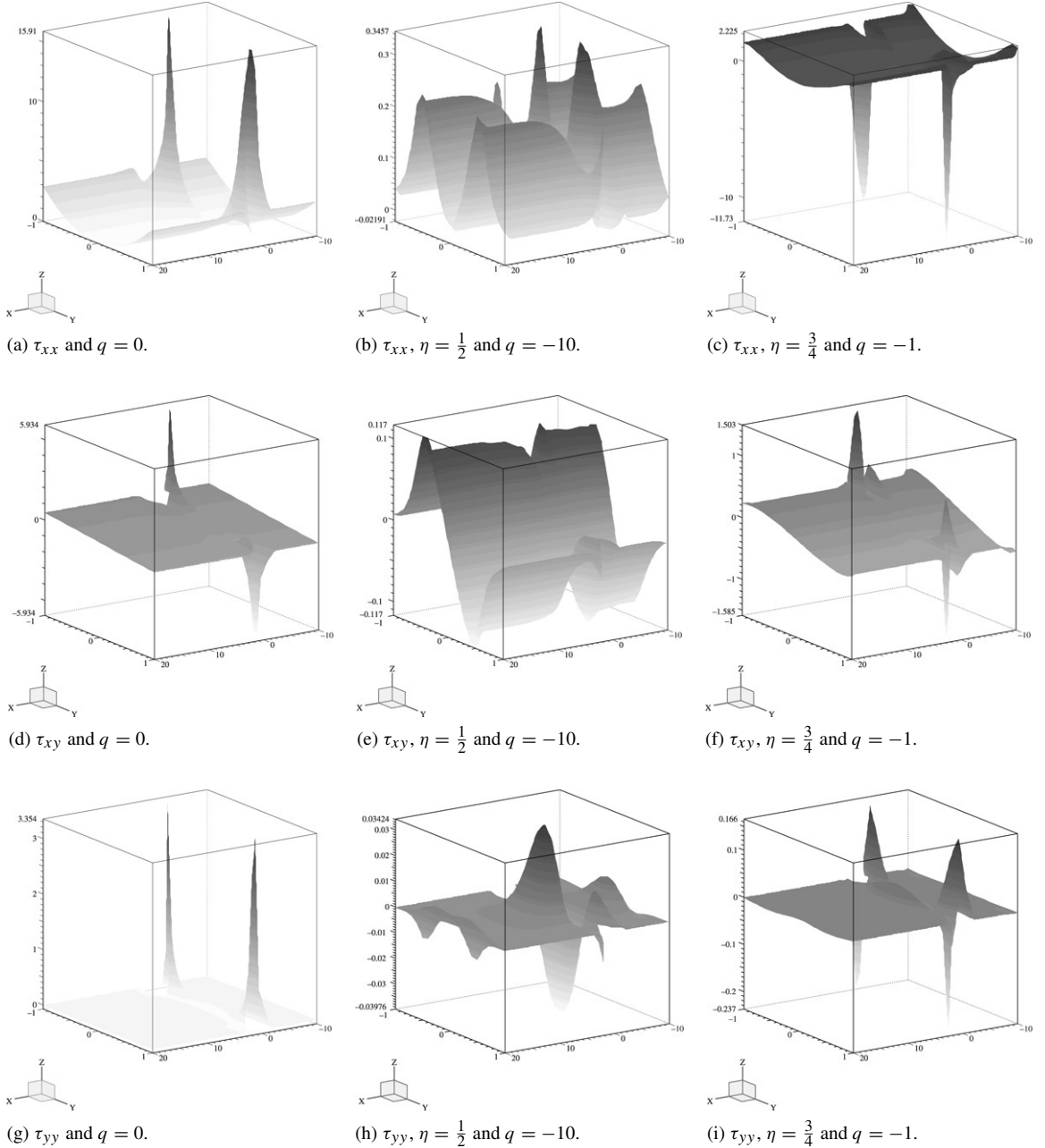


Fig. 12. Viscosity effects on the stress tensor along the stenosis, with $\mathcal{R}e = 30$, $\mathcal{W}e = 3$, $w = \frac{1}{2}$ and different values of the viscosity parameters η and $q \leq 0$.

Remark 4. We notice that the choice of parameters η and w is not independent. This can be easily deduced from the nondimensional governing equations (2.9).

Consider the source term in Eq. (2.9) 3 given by $(w + \eta((1 + |Du|^2)^q - 1))Du$ with $w = 1 - \frac{\lambda_2}{\lambda_1(v + v_0)}$ and $\eta = \frac{v_0}{v + v_0}$.

Denoting $x = |Du|$ and $A = (w + \eta((1 + |Du|^2)^q - 1))Du$ it follows that

$$A = w + \eta((1 + x^2)^q - 1) \geq 0 \Leftrightarrow (1 + x^2)^q \geq \frac{\eta - w}{\eta}. \quad (4.4)$$

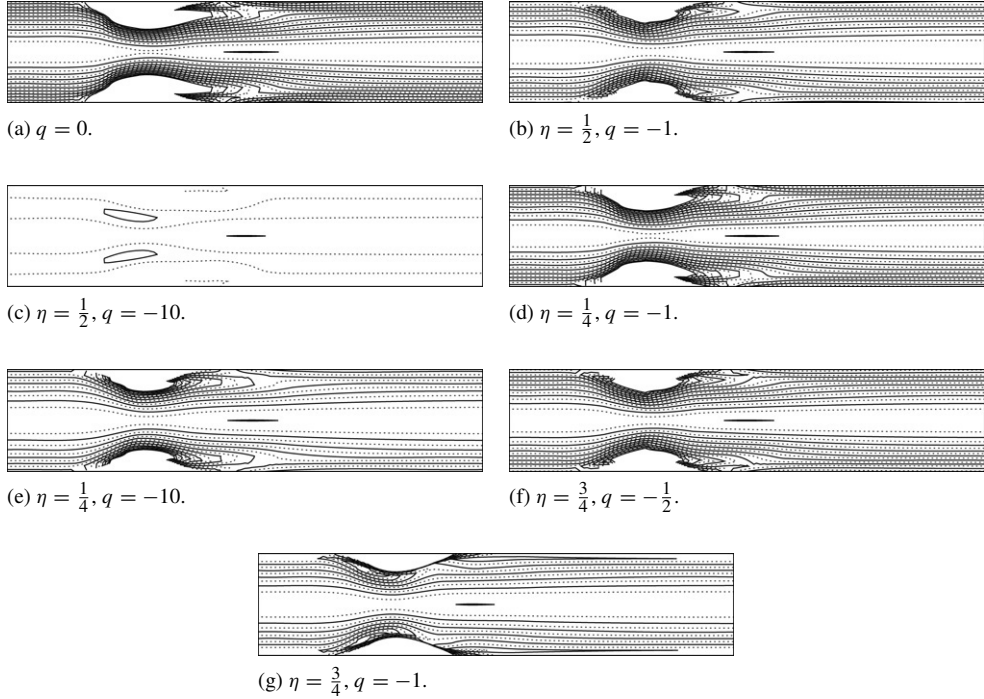


Fig. 13. Viscosity effects on the isovales of the stress component τ_{xx} along the stenosis, with $\mathcal{R}e = 30$, $\mathcal{W}e = 3$, $w = \frac{1}{2}$ and different values of the viscosity parameters η and $q \leq 0$.

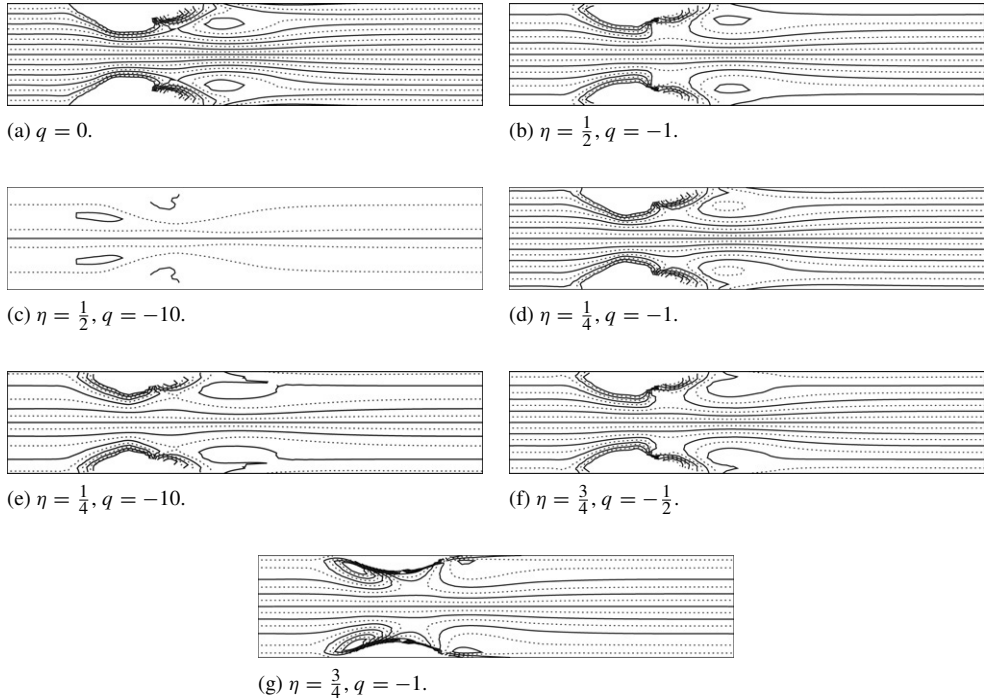


Fig. 14. Viscosity effects on the isovales of the stress component $\tau_{xy} = \tau_{yx}$ along the stenosis, with $\mathcal{R}e = 30$, $\mathcal{W}e = 3$, $w = \frac{1}{2}$ and different values of the viscosity parameters η and $q \leq 0$.

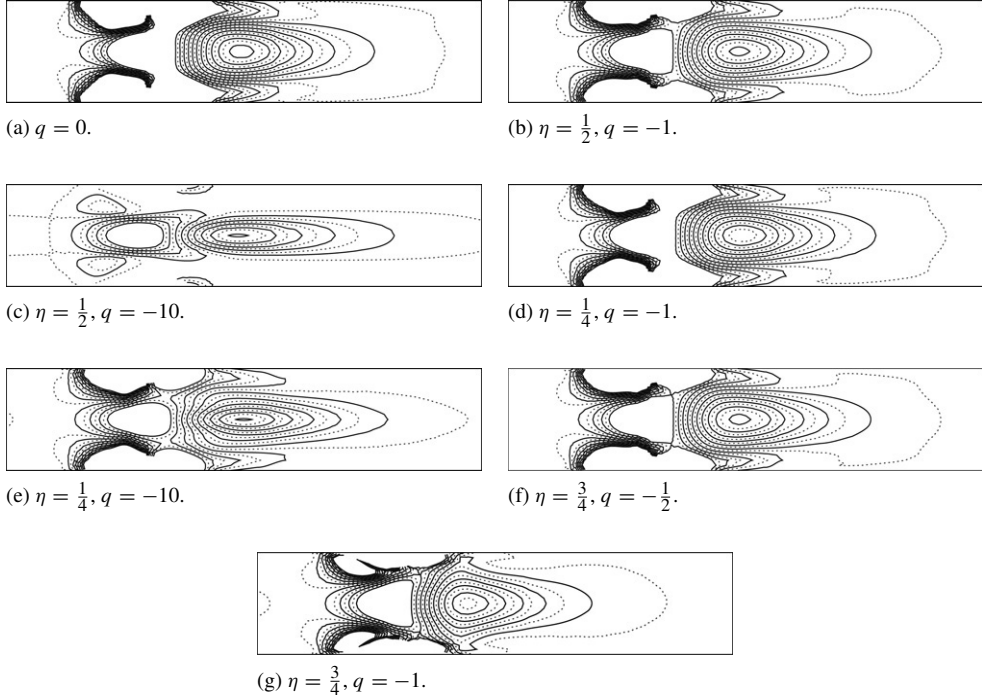


Fig. 15. Viscosity effects on the isovales of the stress component τ_{yy} along the stenosis, with $\mathcal{Re} = 30$, $\mathcal{We} = 3$, $w = \frac{1}{2}$ and different values of the viscosity parameters η and $q \leq 0$.

If $\eta - w \leq 0$, inequality (4.4) is verified for any values of q and x . However, for $\eta - w > 0$ we get

$$\begin{cases} A \geq 0 \Leftrightarrow q \geq \frac{\ln\left(\frac{\eta-w}{\eta}\right)}{\ln(1+x^2)}, & \text{for all } x \neq 0, \\ A \leq 0 \Leftrightarrow q \leq \frac{\ln\left(\frac{\eta-w}{\eta}\right)}{\ln(1+x^2)}, & \text{for all } x \neq 0. \end{cases} \quad (4.5)$$

Then it follows that the sign of A in the source term is determined by the choice of the parameters η and w . For $\eta = w$ and $\eta < w$, A is positive, for any value of q . However, if $\eta > w$ then the sign of A changes according to (4.5).

Fig. 11 shows the wall shear stress (WSS) distribution on the upper wall of the stenosis for parameters referred above and for different values of the power index $q \leq 0$. We observe the presence of a peak wall shear stress due to the stenosis, for any value of $q \leq 0$. **Fig. 11(a)** and (b) corresponding to $\eta < w$ and $\eta = w$ respectively, show that the peak shear stress value decreases with q , when compared with $q = 0$ (Oldroyd-B fluid). The profiles in **Fig. 11(c)** correspond to the choice $\eta > w$ and show a different peak behavior at the stenosis for $q \leq -\frac{1}{2}$. According to Remark 4 we observe that A is negative for $q = \ln(\frac{4}{5}) \ln^{-1}(1 + |Du|^2)$ which corresponds approximately to $q = -\frac{1}{2}$ in the numerical simulations. Small oscillations of the peak WSS appear for $q = -\frac{1}{2}$ and increase for decreasing values of q . **Fig. 11(d), (e) and (f)** show a similar qualitative behavior when $w = \frac{1}{2}$. We conclude that the negative values of the WSS show the existence of a large zone of recirculation and reversal flow around the stenosis (see e.g. [49]).

The spatial distribution of the stress components around the upper wall of the stenosis is illustrated through the 3D plots of **Fig. 12**, which in particular show the viscosity effects when compared to the reference solution (Oldroyd-B fluid, $q = 0$). When $\eta = w$ (**Fig. 12(b), (e) and (h)**) the stress tensor components present oscillations for small values of the power index q . When $\eta > w$ (**Fig. 12(c), (f) and (i)**) the profile of τ_{xx} shows two negative peaks, upstream and downstream of the stenosis while the peaks of τ_{yy} are reversed. The component τ_{xy} presents a peak value upstream and downstream of the stenosis with opposite signs. **Figs. 13–15** show 2D plots of the stress components around the

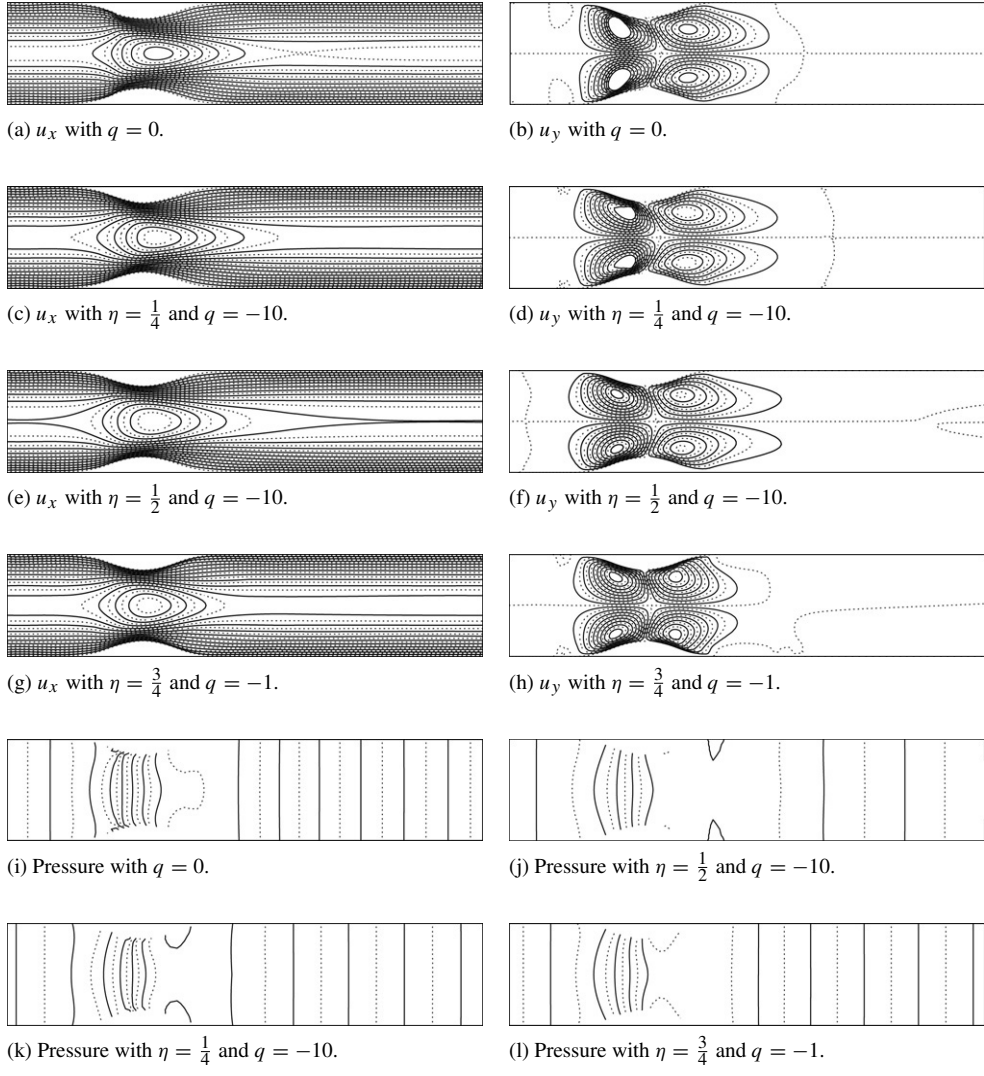


Fig. 16. Isovalues of the velocity and the pressure along the stenosis, with $\mathcal{R}e = 30$, $\mathcal{W}e = 3$, $w = \frac{1}{2}$ and different values of the viscosity parameters η and $q \leq 0$.

stenosis. Viscosity effects are not visible for any considered values of the parameters η and q , except in the case of Figs. 13(c), 14(c) and 15(c) as well in Fig. 14(e) (compared with Fig. 14(a)).

Finally, Fig. 16 shows for the inertial, viscoelastic and viscosity parameters already used, the isovalues of the velocity and pressure fields around the stenosis. When $A \geq 0$ (Fig. 16(c)–(f)) we verify an elongation of the contour lines of the velocity components while for $A < 0$ (Fig. 16(g) and (h)) these isovalues are concentrated in the core of the stenosis.

The present work does not include the study of non-Newtonian viscosity and viscoelastic effects of the model as a function of the stenosis severity for steady or pulsatile flows. Therefore it must be considered as a preliminary step towards the application to blood flow in stenosed vessels.

5. Conclusions

Successful viscoelastic flow simulations require great efforts and much computer resources, mainly due to the hyperbolic character of the constitutive equations. In this paper a hybrid FE/FV numerical method has been developed to solve shear dependent incompressible viscoelastic flows by a generalized Oldroyd-B model with a non-Newtonian viscosity depending on the second invariant of the rate of deformation tensor.

In order to validate the numerical method, the 4:1 planar contraction benchmark problem for creeping flows has been investigated using several refined meshes. The behavior of the re-entrant corner vortex has been analyzed for increasing Weissenberg numbers up to $We = 3$ showing, for the classical Oldroyd-B model, results which are in good agreement with those found in the literature. Interesting viscosity effects have been observed for both shear-thinning and shear-thickening flows, at the re-entrant corner and on both upstream and downstream channels, for certain ranges of the viscosity parameters.

Numerical results have also been obtained for shear-thinning Oldroyd-B fluids in a stenosed channel where interesting combined effects of inertia, viscoelasticity and viscosity have been studied as a function of the corresponding dimensionless parameters.

One of the important features of this analysis is its application to blood flow in small size vessels where the viscosity shear-thinning and nonlinear viscoelastic behavior at low shear rates, should not be neglected [6] as is usually done in large vessels. From this steady flow study of viscosity, pressure and wall shear stress distribution in a rigid stenosed channel, basic characteristics of the complex rheology of blood could be found in relation to the shape of the flow domain since diseased vessels are often relatively rigid. However, for the complete assessment of the shear-thinning and viscoelastic properties of human blood, unsteady flow on a more severe stenotic geometry has to be considered to provide some understanding of the genesis of atherosclerosis and other arterial lesions (see e.g. [37,48–51]). The main objective of future work will be to extend this numerical study to unsteady two dimensional and three dimensional flows in stenotic vessels, under physiological conditions.

Acknowledgments

This work has been partially supported by the Projects POCTI/MAT/41898/2001, HPRN-CT-2002-00270 and by the Center for Mathematics and its Applications — CEMAT/IST through FCT's Funding Program.

References

- [1] K.R. Rajagopal, Mechanics of non-Newtonian fluids, in: G.P. Galdi, J. Nečas (Eds.), Recent Developments in Theoretical Fluid Mechanics, in: Pittman Research Notes in Mathematics Series, vol. 291, Longman's Scientific and Technical, 1993, pp. 129–162.
- [2] D.V. Boger, K. Walters, Rheological Phenomena in Focus, in: Rheology Series, vol. 4, Elsevier, New-York, 1993.
- [3] C. Truesdell, W. Noll, in: S. Flügge (Ed.), The Non-Linear Field Theories of Mechanics, in: Encyclopedia of Physics, vol. III/3, Springer-Verlag, 1965.
- [4] R.B. Bird, R.C. Armstrong, O. Hassager, Dynamics of Polymeric Liquids, John Wiley & Sons, New-York, 1987.
- [5] W.R. Schowalter, Mechanics of Non-Newtonian Fluids, Pergamon Press, New-York, 1978.
- [6] G.B. Thurston, Viscoelasticity of human blood, *Biophys. J.* 12 (1972) 1205–1217.
- [7] K.K. Yelavarapu, M.V. Kameneva, K.R. Rajagopal, J.F. Antaki, The flow of blood in tubes: Theory and experiment, *Mech. Res. Comm.* 3 (25) (1998) 257–262.
- [8] K.R. Rajagopal, A. Srinivasa, A thermodynamic framework for rate type fluid models, *J. Non-Newtonian Fluid Mech.* 88 (2000) 207–228.
- [9] M. Anand, K.R. Rajagopal, A shear-thinning viscoelastic fluid model for describing the flow of blood, *Int. J. Cardiovascular Medicine Sci.* 4 (2004) 59–68.
- [10] R. Keunings, A survey of computational rheology, in: D.M. Binding, et al. (Eds.), Proceedings of the XII International Congress of Rheology, in: British Soc. Rheol., vol. 1, 2000, pp. 7–14.
- [11] M.J. Crochet, A.R. Davis, K. Walters, Numerical Simulation of Non-Newtonian Flow, Elsevier, New-York, 1984.
- [12] R. Owens, T.N. Phillips, Computational Rheology, Imperial College Press, London, 2002.
- [13] F.P.T. Baaijens, Mixed finite element methods for viscoelastic flow analysis: A review, *J. Non-Newtonian Fluid Mech.* 79 (1998) 361–385.
- [14] J.M. Marchal, M.J. Crochet, A new mixed finite element for calculation of viscoelastic flow, *J. Non-Newtonian Fluid Mech.* 26 (1987) 77–114.
- [15] M. Fortin, R. Pierre, On the convergence of the mixed method of Crochet and Marchal for viscoelastic flows, *Comput. Methods Appl. Mech. Eng.* 73 (1989) 341–350.
- [16] X.L. Luo, R.I. Tanner, A decoupled finite element streamline-upwind scheme for viscoelastic flow problems, *J. Non-Newtonian Fluid Mech.* 31 (1989) 143–162.
- [17] V.J. Ervin, W.W. Miles, Approximation of time-dependent viscoelastic fluid flow: SUPG approximation, *SIAM J. Numer. Anal.* 41 (2) (2003) 457–486.
- [18] A. Fortin, M. Fortin, A new approach for the finite element simulation of viscoelastic fluid flows, *J. Non-Newtonian Fluid Mech.* 32 (1989) 295–310.
- [19] P. Saramito, Efficient simulation of nonlinear viscoelastic fluid flows, *J. Non-Newtonian Fluid Mech.* 60 (1995) 199–223.
- [20] J. Baranger, S. Wardi, Numerical analysis of a FEM for transient viscoelastic flow, *Comput. Methods Appl. Mech. Eng.* 125 (1995) 171–185.
- [21] M. Fortin, D. Esselaoui, A finite element procedure for viscoelastic flows, *Int. J. Numer. Meth. Fluids* 7 (1987) 1035–1052.
- [22] O. Pironneau, On the transport-diffusion algorithm and its application to the Navier–Stokes equations, *Numer. Math.* 38 (1982) 309–332.

- [23] S.V. Patankar, Numerical Heat Transfer and Fluid Flow, in: Series in Computational Methods in Mechanics and Thermal Sciences, Hemisphere Publishing Corporation, 1980.
- [24] J.Y. Yoo, Y. Na, A numerical study of the planar contraction flow of viscoelastic fluid using the SIMPLER algorithm, *J. Non-Newtonian Fluid Mech.* 39 (1) (1991) 89–106.
- [25] G.P. Sasikal, A finite volume approach for calculation of viscoelastic flow through an abrupt axisymmetric contraction, *J. Non-Newtonian Fluid Mech.* 56 (1995) 15–47.
- [26] S.C. Xue, N. Phan-Thien, R.I. Tanner, Upwinding with deferred correction (UPDC) an effective implementation of higher-order convection schemes for implicit finite volume methods, *J. Non-Newtonian Fluid Mech.* 108 (1) (2002) 1–24.
- [27] H. Al Moatssime, D. Esselaoui, A. Hakim, S. Raghay, Finite volume multigrid method of the planar contraction flow of a viscoelastic fluid, *Int. J. Numer. Meth. Fluids* 36 (2001) 885–902.
- [28] T.N. Phillips, A.J. Williams, Comparison of creeping and inertial flow of an Oldroyd-B fluid through planar and axisymmetric contractions, *J. Non-Newtonian Fluid Mech.* 108 (2002) 25–47.
- [29] H.S. Dou, N. Phan-Thien, The flow of an Oldroyd-B fluid past a cylinder in a channel: Adaptive viscosity vorticity (DAVSS- ω) formulation, *J. Non-Newtonian Fluid Mech.* 87 (1) (1999) 47–73.
- [30] P.J. Oliveira, F.T. Pinho, Plane contraction flows of upper convected Maxwell and Phan-Thien–Tanner fluids as predicted by a finite-volume method, *J. Non-Newtonian Fluid Mech.* 88 (1) (1999) 63–88.
- [31] M.A. Alves, F.T. Pinho, P.J. Oliveira, The flow of viscoelastic fluids past a cylinder: Finite-volume high-resolution methods, *J. Non-Newtonian Fluid Mech.* 97 (2001) 207–232.
- [32] S.S. Edussuriya, A.J. Williams, C. Bailey, A cell-centered finite volume method for modelling viscoelastic flow, *J. Non-Newtonian Fluid Mech.* 117 (1–2) (2004) 47–61.
- [33] T. Sato, S.M. Richardson, Explicit numerical simulation of time-dependent viscoelastic flow problems by finite element/finite volume method, *J. Non-Newtonian Fluid Mech.* 51 (3) (1994) 249–275.
- [34] P. Wapperom, M.F. Webster, A second-order hybrid finite element/volume method for viscoelastic flows, *J. Non-Newtonian Fluid Mech.* 2–3 (79) (1998) 405–431.
- [35] N. Arada, A. Sequeira, Strong steady solutions for a generalized Oldroyd-B model with shear-dependent viscosity in a bounded domain, *Math. Models Methods Appl. Sci.* 13 (9) (2003) 1303–1323.
- [36] S.A. Berger, L.D. Jou, Flows in stenotic vessels, *Annu. Rev. Fluid Mech.* 32 (2000) 347–382.
- [37] C.G. Caro, T.J. Pedley, R.C. Schroter, W.A. Seed, *The Mechanics of the Circulation*, Oxford Univ. Press, 1978.
- [38] F. Brezzi, M. Fortin, *Mixed and Hybrid Finite Element Methods*, Springer-Verlag, 1991.
- [39] V. Girault, P.A. Raviart, *Finite Element Methods for Navier–Stokes Equations. Theory and Algorithms*, in: Springer Series in Computational Mathematics, Springer-Verlag, Berlin, Heidelberg, 1986.
- [40] P.J. Oliveira, F.T. Pinho, G.A. Pinto, Numerical simulation of nonlinear elastic flows with a general collocated finite volume method, *J. Non-Newtonian Fluid Mech.* 79 (1) (1998) 1–43.
- [41] M. Aboubacar, M.F. Webster, Development of an optimal hybrid finite volume/element method for viscoelastic flows, *Int. J. Numer. Meth. Fluids* 41 (11) (2003) 1147–1172.
- [42] J.H. Ferziger, M. Perić, *Computational Methods for Fluid Dynamics*, 3rd ed., Springer-Verlag, Berlin, Heidelberg, New York, 2002.
- [43] J.M. Thomas, D. Trujillo, Mixed finite volume methods, *Int. J. Numer. Meth. Eng.* 46 (1999) 1351–1366.
- [44] H.P. Langtangen, *Computational Partial Differential Equations — Numerical Methods and Diffpack Programming*, 2nd ed., Springer-Verlag, 2002.
- [45] I.J. Keshtiban, F. Belblidia, M.F. Webster, Computation of incompressible and weakly-compressible viscoelastic liquids flow: Finite element/volume schemes, *J. Non-Newtonian Fluid Mech.* 126 (2005) 123–143.
- [46] P. Saramito, *Simulation Numérique d’Ecoulements de Fluides Viscoélastiques par Éléments Finis Incompressibles et une Méthode de Directions Alternées - Applications*, Thèse de doctorat, IMG-INPG, Université Joseph Fourier, 1990.
- [47] A.E. Caola, Y.L. Loo, R.C. Armstrong, R.A. Brown, Highly parallel time integration of viscoelastic flows, *J. Non-Newtonian Fluid Mech.* 100 (2001) 191–216.
- [48] A.M. Malek, S.L. Alper, S. Izumo, Hemodynamic shear stress and its role in atherosclerosis, *JAMA* 282 (1999) 2035–2042.
- [49] J.R. Buchanan Jr., C. Kleinstreuer, J.K. Comer, Rheological effects on pulsatile hemodynamics in a stenosed tube, *Comput. Fluids* 29 (2000) 695–724.
- [50] P. Neofytou, D. Drikakis, Effects of blood models on flows through stenosis, *Int. J. Numer. Meth. Fluids* 43 (2003) 597–635.
- [51] W.L. Siauw, E.Y.K. Ng, J. Mazumdar, Unsteady stenosis flow prediction: A comparative study of non-Newtonian models with operator splitting scheme, *Medical Eng. Phys.* 22 (2000) 265–277.